Separating the effects of nucleotide and EB binding on microtubule structure

Rui Zhang[a,b,1,2], Benjamin LaFrance[c], and Eva Nogales[a,b,d,2]

[a]Molecular Biophysics and Integrated Bioimaging Division, Lawrence Berkeley National Laboratory, Berkeley, CA 94720; [b]Department of Molecular and Cell Biology, University of California, Berkeley, CA 94720; [c]Molecular and Cell Biology Graduate Program, University of California, Berkeley, CA 94720; and [d]Howard Hughes Medical Institute, University of California, Berkeley, CA 94720

Contributed by Eva Nogales, May 30, 2018 (sent for review February 13, 2018; reviewed by Gary Brouhard and Carolyn A. Moores)

Microtubules (MTs) are polymers assembled from αβ-tubulin heterodimers that display the hallmark behavior of dynamic instability. MT dynamics are driven by GTP hydrolysis within the MT lattice, and are highly regulated by a number of MT-associated proteins (MAPs). How MAPs affect MTs is still not fully understood, partly due to a lack of high-resolution structural data on undecorated MTs, which need to serve as a baseline for further comparisons. Here we report three structures of MTs in different nucleotide states (GMPCPP, GDP, and GTPγS) at near-atomic resolution and in the absence of any binding proteins. These structures allowed us to differentiate the effects of nucleotide state versus MAP binding on MT structure. Kinesin binding has a small effect on the extended, GMPCPP-bound lattice, but hardly affects the compacted GDP-MT lattice, while binding of end-binding (EB) proteins can induce lattice compaction (together with lattice twist) in MTs that were initially in an extended and more stable state. We propose a MT lattice-centric model in which the MT lattice serves as a platform that integrates internal tubulin signals, such as nucleotide state, with outside signals, such as binding of MAPs or mechanical forces, resulting in global lattice rearrangements that in turn affect the affinity of other MT partners and result in the exquisite regulation of MT dynamics.

microtubule | dynamic instability | EB proteins | kinesin | nucleotide

Microtubules (MTs) are hollow tubes composed of αβ-tubulin heterodimers that stack head-to-tail to form linear protofilaments (PFs), which in turn associate laterally to define a cylindrical wall. In most eukaryotic cells, 13-PF MTs are the dominant form (1, 2), although MTs with different PF numbers have been reported for certain species (3). The prevalence of 13-PFs in vivo could be due to the fact that MTs are typically nucleated from γ-tubulin ring complex (γ-TuRC) (4–6), which has been proposed as a template for 13-PF MT, or because MTs assemble in the presence of MT-associated proteins (MAPs), such as end-binding proteins (EBs) and doublecortin, that bind across PFs and strongly promote the formation of 13-PF MTs, as observed in vitro (7–10). Budding yeast MTs assemble predominantly as 12-PFs in vitro, but also shift toward 13-PFs in the presence of either Bim1 (yeast homolog of EB) or mammalian EBs (11, 12). It has also been proposed that tubulin isoforms and posttranslational modifications of tubulin are important determinants of MT geometry (3), but it is unclear whether these factors directly influence MT structure or whether they do so indirectly, by defining the set of MAPs that interact with the MT.

Most MTs, whether assembled in vitro or in vivo, have a "seam" (13–16), where the lateral interactions between PFs are heterotypic (α-tubulin interacts with β-tubulin), whereas the rest of the MT has homotypic lateral interactions (α–α or β–β contacts). It is unclear what the physiological relevance of the seam is, although roles in MT growth and shrinkage have been proposed (13). The MT seam has also been suggested to provide a unique binding site for MAPs (8, 13, 17), although no seam-binding protein has been identified yet. More recently, other biological systems that also possess a seam have been reported, such as a "mini-microtubule" (18) and a flagellar filament (19) found in bacteria.

αβ-Tubulin forms a stable heterodimer following its biogenesis, with each subunit bound to a guanine nucleotide (20, 21). The GTP bound at the N-site (nonexchangeable site on α-tubulin) is always buried at the α–β interface within the dimer, is never hydrolyzed, and plays a purely structural role (22). The GTP bound to the E-site (exchangeable site on β-tubulin), on the other hand, can be exchanged in unpolymerized tubulin dimers and is hydrolyzed to GDP within the MT following dimer addition to the lattice (23). This hydrolysis results in MTs that are highly dynamic and undergo stochastic switches between growth and shrinkage phases, the hallmark phenomenon known as dynamic instability (24). MTs will continue to grow as long as there is a cap of GTP-bound tubulin at their ends (25, 26), but losing this GTP-cap makes the MT unstable and prone to depolymerization. Highlighting the importance of MT dynamics, the leading anticancer drug Taxol inhibits cell division by stabilizing MTs and suppressing their dynamic properties (27–29).

Significance

We report three high-resolution structures of microtubules in different nucleotide states—GMPCPP, GDP, and GTPγS—in the absence of any binding proteins, allowing us to separate the effects of nucleotide- and microtubule (MT)-associated protein (MAPs) binding on MT structure. End-binding (EB) proteins can bind and induce partial lattice compaction of a preformed GMPCPP-bound MT, a lattice type that is far from EBs' ideal binding platform. We propose a model in which the MT lattice serves as a platform that integrates internal tubulin signals, such as nucleotide state, with outside signals, such as binding of MAPs. These global lattice rearrangements in turn affect the affinity of other MT partners and result in the exquisite regulation of the MT dynamics.

Author contributions: R.Z. and E.N. designed research; R.Z. and B.L. performed research; R.Z., B.L., and E.N. analyzed data; and R.Z., B.L., and E.N. wrote the paper.

Reviewers: G.B., McGill University; and C.A.M., Institute of Structural and Molecular Biology.

The authors declare no conflict of interest.

Data deposition: The cryo-EM maps have been deposited in the Electron Microscopy Data Bank (EMDB) [undecorated GMPCPP-MT (EMD-7973), undecorated GDP-MT GMPCPP-MT (EMD-7974), undecorated GTPγS-MT (EMD-7975), and EB3-washed GMPCPP-MT, class 1 and 2 (EMD-7976 and EMD-7977)]. The refined atomic models for the undecorated GMPCPP-, GDP-, and GTPγS-MT have been deposited in the Protein Data Bank (PDB) (PBD ID codes 6DPU, 6DPV, and 6DPW, respectively).

[1]Present address: Department of Biochemistry and Molecular Biophysics, Washington University in St. Louis, School of Medicine, St. Louis, MO 63110.

[2]To whom correspondence may be addressed. Email: zhangrui@wustl.edu or enogales@lbl.gov.

This article contains supporting information online at www.pnas.org/lookup/suppl/doi:10.1073/pnas.1802637115/-/DCSupplemental.

Published online June 18, 2018.

Recently, high-resolution cryo-electron microscopy (cryo-EM) allowed us to directly visualize MTs in different nucleotide states with unprecedented detail (30, 31). Comparison of MTs bound to GDP and the slowly hydrolyzable GTP analog GMPCPP (which mimics the GTP state at growing MT ends; see *Discussion*) revealed an ∼2-Å lattice compaction occurring at the interface between tubulin dimers that is mainly due to conformational changes in α-tubulin. We proposed that this lattice compaction generates strain inside the MT lattice that will ultimately be released upon MT depolymerization (30, 31). It is worth noting that these cryo-EM studies used a bound kinesin motor as a fiducial marker on the MT to distinguish between the highly similar α- and β-tubulin structures during image analysis. This fact left open the possibility that kinesin itself could influence MT structure, complicating the interpretation of the observed effects attributed to GTP hydrolysis.

MT dynamics are highly regulated by a number of MAPs. Among them is a family of proteins named plus-end tracking proteins (+TIPs), which selectively accumulate at the growing ends of MTs (32). The EB proteins mentioned above are the central hub of the +TIPs network, and many other +TIPs hitchhike on EBs to track with the MT-plus ends (33). Recent studies showed that EBs influence MT dynamics by promoting MT growth, but also by increasing the frequency of catastrophes, the switch from MT growth to shrinkage (10, 34). In vitro, EB proteins bind with high affinity to GTPγS-MTs (10, 35), suggesting that GTPγS-MTs may mimic some unique structural feature at the growing end of MTs. Recently, we reported the high-resolution structure of EB3-decorated GTPγS-MT showing a compacted MT lattice with a twist that is different from either the GMPCPP- or GDP-MT state (31). However, it was unclear whether this unique MT lattice was a result of the nucleotide state (GTPγS) or the EB binding. We also showed that through copolymerization with GMPCPP-bound tubulin, EB3 promoted both the rapid hydrolysis of this slowly hydrolyzable GTP analog within the MT lattice, and the accompanying lattice compaction (31). A similar effect was observed for the budding yeast EB3 homolog, Bim1, which also induced lattice compaction for the otherwise extended dynamic budding yeast MTs (11, 12).

Here we report three high-resolution structures of MTs in different nucleotide states—GMPCPP, GDP, and GTPγS—in the absence of any binding proteins. These structures of undecorated MTs posed technical challenges that we have only recently been able to overcome (36), allowing us to separate the effects of nucleotide and MAP binding on MT structure. We also demonstrate that, at high concentrations, EBs can bind and induce partial lattice compaction of a preformed 14-PF GMPCPP-MT, a MT lattice type that is far from EBs' ideal binding platform, further supporting our previous model that EB binding alters the MT lattice (31).

Results

Structures of Undecorated GMPCPP- and GDP-MTs. We recently developed a cryo-EM data-processing protocol that is able to rely on small structural differences between α- and β-tubulin to determine the correct αβ-tubulin register and seam location in MT images. The protocol considers all possible MT-symmetry–related solutions during image alignment, then selects the best match to the experimental image (36). This protocol overcomes the need of a tubulin dimer marker, such as a kinesin or EB (10, 15, 16, 30, 31), and works well even for undecorated MTs. The success of the protocol is demonstrated by the clear distinction between α- and β-tubulin densities in the resulting cryo-EM reconstructions (Fig. 1*A*). For example, the S9-S10 loop, which is longer in α-tubulin, is clearly resolved and easily distinguished between α- and β-tubulin (Fig. 1*B*). It is also reflected by the correct seam configuration displayed in the asymmetric (C1) reconstruction: that is, without application of pseudohelical symmetry (Fig. 1*C*). Using this data-processing protocol, we have now determined the structures of undecorated GMPCPP- and GDP- MTs at atomic resolution (*SI Appendix*, Table S1). In both datasets, 14-PF MTs were the dominant form (*SI Appendix*, Fig. S1).

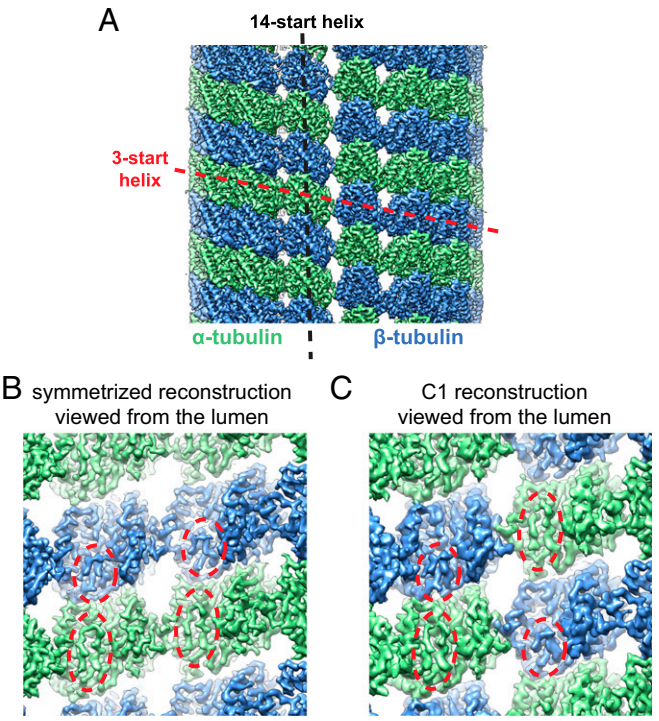

Fig. 1. High-resolution structure of undecorated MTs. (*A*) Surface rendering of a cryo-EM density map of undecorated GMPCPP-MT with pseudohelical symmetry applied. The α- and β-tubulin are colored in green and blue, respectively, throughout the report, unless specified. The red and black dash lines denote the 3-start and 14-start (or 13-start, in the case of 13-PF MT) helices of the MT, respectively. (*B*) Zoomed-in view of the cryo-EM reconstruction in *A*, viewed from the lumen. The red dashed circles highlight the density region corresponding to the S9-S10 loop, which has different lengths in α- and β-tubulin. (*C*) Zoomed-in view (from the lumen) of the corresponding C1 reconstruction of undecorated GMPCPP-MT without applied pseudohelical symmetry, showing the configuration at the seam.

For further quantitative analysis of the MT structure, we considered two helical parameters, the "dimer rise" and the "dimer twist," to describe the MT lattice in different conditions. The dimer rise and dimer twist are defined as a set of translational and rotational operations that relates one tubulin dimer (i.e., one MT asymmetric unit) to the adjacent tubulin dimer within the same PF (Fig. 2*A*). In other words, they are helical parameters for the 14-start (or 13-start, for a 13-PF MT) helix of the MT (Fig. 1*A*). Another set of parameters we find useful in describing a certain MT lattice are the intra- and interdimer distances (Fig. 2*B*). The intradimer distance is defined as the distance between two tubulin subunits sandwiching the nonhydrolyzable GTP at the N-site, while the interdimer distance is that between two tubulin subunits sandwiching the exchangeable nucleotide at the E-site.

Upon comparing undecorated MTs with our previously reported kinesin-decorated MTs (30, 31) (Fig. 2 *C* and *D* and *SI Appendix*, Table S2), we find that kinesin-1 binding shortens the spacing between longitudinally interacting tubulin dimers (the dimer rise) of the GMPCPP-MT by 0.7 Å. Interestingly, the spindle assembly factor TPX2 has the opposite effect on the GMPCPP-MT, slightly increasing the dimer rise by 0.3 Å (37). On the other hand, kinesin-1 binding hardly affects the lattice spacing of the already compacted GDP-MT. Similarly, kinesin-1 binding has a small shortening effect on the dimer rise of EB3-decorated GDP-MT (0.1 Å) or EB3-decorated GTPγS-MT (0.4 Å), with the caveat that EB3 binding

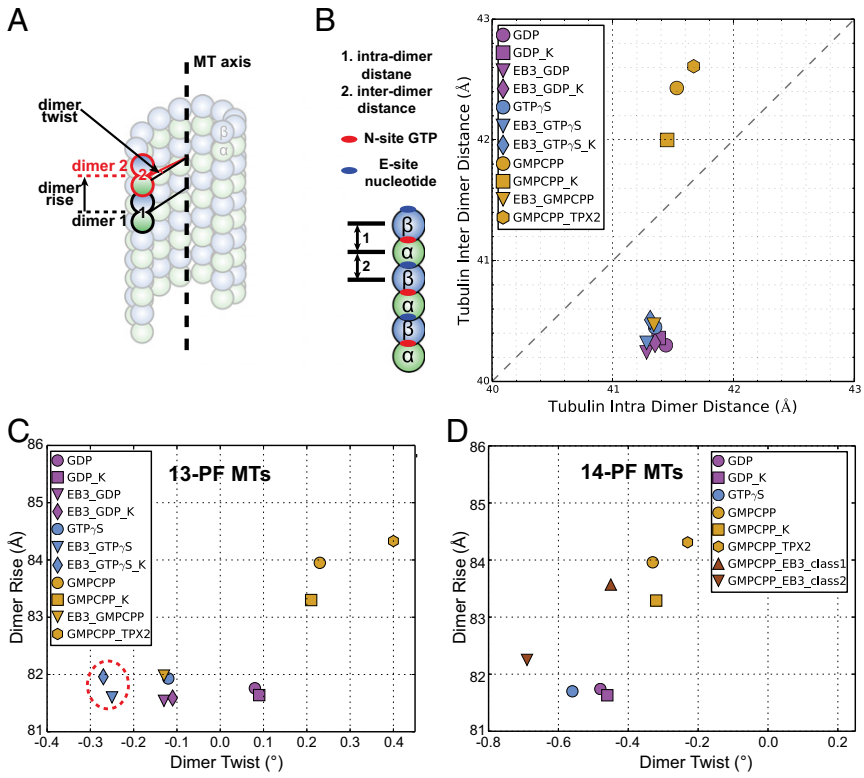

Fig. 2. Variation of lattice parameters for different MT states. (*A*) The MT dimer rise and dimer twist are defined as the translational and rotational operations that relate one tubulin dimer (dimer 1, outlined in black) to the adjacent tubulin dimer (dimer 2, outlined in red) along the same PF. The dimer rise and twist are measured directly from the C1 reconstruction of each MT state (*SI Appendix*, Table S2). (*B*) Plot of interdimer vs. intradimer distances for each MT state. Here the interdimer distance is defined as the distance between two tubulin subunits sandwiching the exchangeable nucleotide at the E-site, while the intradimer distance is the distance between two tubulin subunits sandwiching the nonhydrolyzable GTP. The values of the interdimer and intradimer distances were calculated from the atomic models of each state, using the mean of the Cα distances between α- and β-tubulin for each pair of corresponding residues. (*C*) Plot of dimer rise versus dimer twist for 13-PF MTs in different states. The red dashed circle indicates the values corresponding to the optimal MT lattice for EB3 binding. (*D*) Plot of dimer rise versus dimer twist for 14-PF MTs in different states. In the figure legend, if the name of the binding protein comes before the nucleotide (e.g., EB3-GMPCPP), then the MTs were polymerized in the presence of the binding protein. If the name of the binding protein comes after the nucleotide (e.g., GMPCPP-EB3), then the protein was added to preformed MTs. "K" denotes kinesin. This nomenclature is used consistently throughout the report.

is reduced in the presence of the kinesin due to a small overlap of the two binding sites on the MT surface (31). The dimer rise of the undecorated GDP-MT is also very similar to that of the EB3-decorated GDP-MT, suggesting that GDP-MT may represent the most compacted state of the MT, likely corresponding to the tubulin conformation storing the largest amount of strain within the lattice (31, 38). It should be noted that among all of the MT states we visualized, the intradimer distance remained relatively unchanged, presumably due to the constant presence of GTP at the N-site (Fig. 2*B* and *SI Appendix*, Table S2).

As shown in one of our previous studies, a straightforward method to detect a deviation from a true cylindrical arrangement in the MT is to superimpose the atomic models fitted into the C1 and into the symmetrized reconstructions (31). Following this procedure, we found that in the 13-PF GDP-MT, the two PFs across the seam are significantly further apart from each other than the PFs in the rest of the MT (Fig. 3*A*). This deformation at the seam is also the case for the 14-PF GDP-MT, but to a lesser extent (Fig. 3*B*). The seam opening for 13-PF GDP-MTs is also apparent by directly superimposing the densities of the C1 and symmetrized reconstructions (Fig. 3*C*). In both the 13-PF and 14-PF GMPCPP-MTs, the position of the two PFs across the seam is almost identical for the C1 and the symmetrized reconstructions (Fig. 3 *D* and *E*). Previously, we reported a slight seam opening for the 13-PF kinesin-decorated GMPCPP-MTs (Fig. 3*F*) (31). We can now attribute this difference to kinesin-1 binding, which changes the lattice spacing of GMPCPP-MT (Fig. 2 *C* and *D* and *SI Appendix*, Table S2), therefore altering the lateral interactions between PFs at the seam.

Structures of Undecorated GTPγS-MT. In previous work, we obtained the high-resolution structure of EB3-decorated GTPγS-MTs, which was polymerized from GMPCPP-MT seeds through coassembly with EB3 (31). However, at that time we were not able to assemble GTPγS-MTs in the absence of EB3. Recently, we improved the experimental protocol by significantly reducing the concentration of Mg^{2+} in the buffer and increasing the starting tubulin concentration and the polymerization time. With these modifications, we obtained a considerable amount of GTPγS-MT extensions out of the GMPCPP-MT seeds without needing to copolymerize with EBs. Consistent with previous reports (35, 39, 40), no MT growth was observed in the absence of GMPCPP-MT seeds, supporting the idea that GTPγS-tubulin is a poor MT nucleator.

In the absence of EB proteins, the GTPγS-MT extensions follow the geometry (i.e., the PF number) of the GMPCPP-MT seeds, which are predominantly 14-PF (~80%) (*SI Appendix*, Fig. S1). This is in stark contrast to the GTPγS-MTs copolymerized with high concentrations of EB3 (also requiring the seeds), which strongly promotes 13-PF MTs (31) (*SI Appendix*, Fig. S1). After sorting out 13- and 14-PF MTs, we used two different image-classification strategies to further separate the GMPCPP-MT seeds from the GTPγS-MT extensions. First, we classified the MT segments by

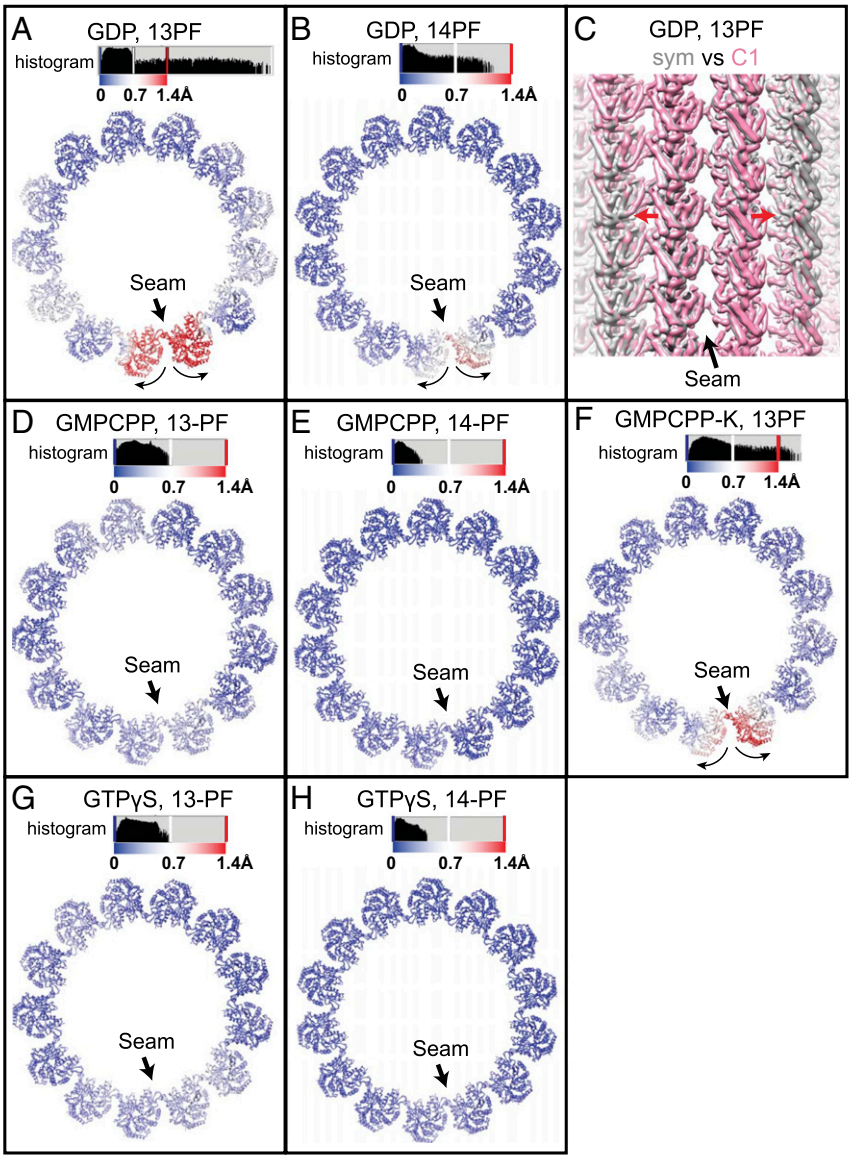

Fig. 3. Lateral contacts at the MT seam for MTs with different stabilities. The panels show comparisons of the C1 and the symmetrized reconstructions of different MT states. (*A*, *B*, and *D*–*H*) Cα-atoms displacements between atomic models of one helical turn of tubulin dimers for the C1 and the symmetrized reconstructions of different MT states, with deviations colored from blue to red. The histograms of Cα-atoms displacements are also shown above the atomic models. (*C*) Superimposition of the C1 and the symmetrized reconstructions of 13-PF GDP MT, showing the seam opening in the C1 reconstruction (red arrows). Both reconstructions have been low-pass–filtered to 7-Å resolution for easier comparison.

measuring their lattice spacing using their layer lines in Fourier space (*Experimental Procedures*). This layer-line analysis showed a bimodal distribution, with one mode corresponding to the peak observed for pure undecorated GMPCPP-MTs and the other mode corresponding to GDP-MTs (Fig. 4*A*). A local average of seven adjacent segments, which significantly increases the signal-to-noise ratio (36), was used for this measurement. In addition, we also performed multireference sorting using two models with different MT lattice types (an extended GMPCPP-MT and a compacted GDP-MT) from our previous studies (31). These two methods gave very consistent classification results, producing two major classes for both 13- and 14-PF MTs. One of the classes (class 1, which contains about 25% of the total particles) had exactly the same lattice parameters as we see for the undecorated GMPCPP-MT (Fig. 4*B*), and therefore should correspond to the GMPCPP-MT seeds. Class 2, which contains 75% of the total particles, had a compacted lattice (Fig. 4*B*), very similar to the previously reported EB3-decorated GTPγS-MT, but with a lesser amount of lattice twist (as measured by dimer twist) (Fig. 2*D*). This class should therefore correspond to the GTPγS-MT extensions. Typically, all of the particles from the same MT are classified into the same class. Although the field-of-view that we used for high-resolution imaging is relatively small, we did occasionally capture transitions between GMPCPP-MT seeds and GTPγS-MT extensions. As a control, we also applied the same multireference sorting protocols to the pure, undecorated GMPCPP-MT and GDP-MT datasets and, in each case, we obtained only one major class containing over 98% of the particles.

With regards to the lateral interactions between PFs across the seam, the C1 and symmetrized reconstructions for the undecorated GTPγS-MT were markedly similar for both 13-PFs and 14-PFs (Fig. 3 *G* and *H*). This result parallels our observations for GMPCPP-MTs (Fig. 3 *D* and *E*). In contrast, the two PFs across the seam are further apart from each other in the GDP-MT, especially

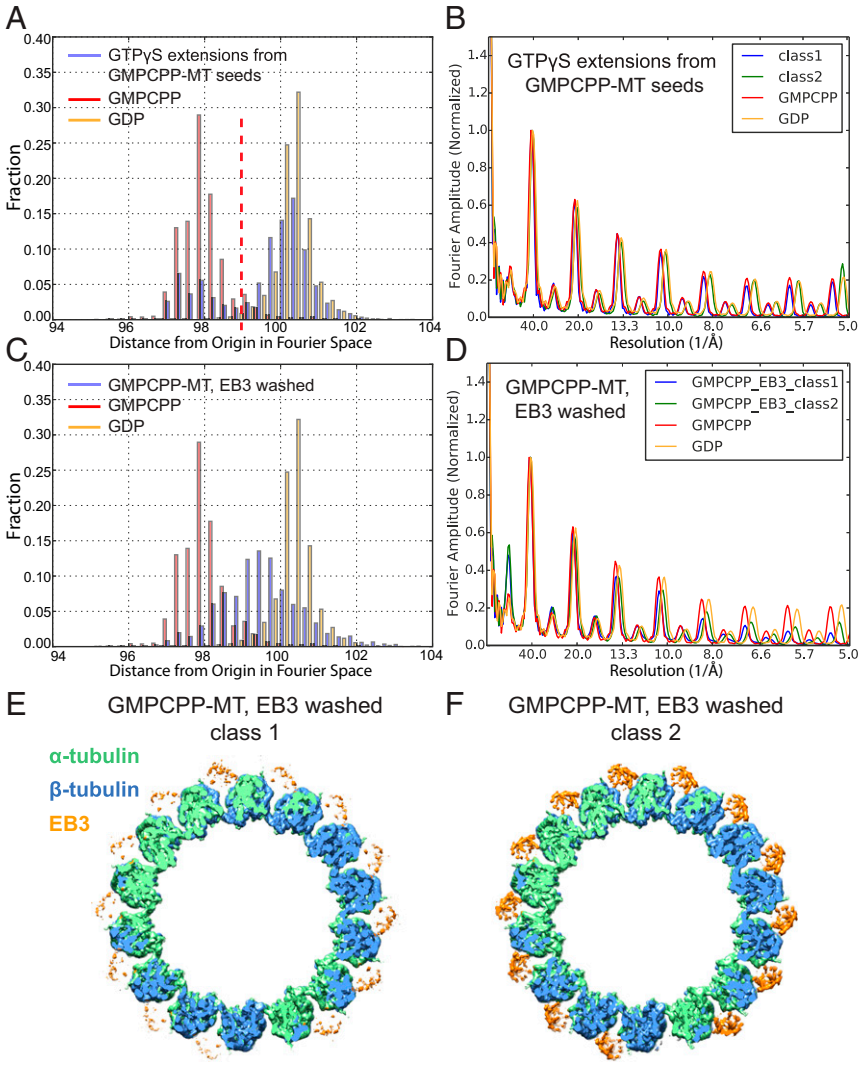

Fig. 4. Separation of different MT lattice types for samples with a mixed population. (*A*) Histogram of layer line positions for each MT segment in the dataset of GTPγS growing from GMPCPP-MT seeds, showing a bimodal distribution (only 14-PF MTs are plotted in blue). The *x*-axis Fourier space unit is arbitrary. The red dashed line indicates the cut-off value we used to separate this dataset into two classes. The histograms of layer line positions for each MT segment in the datasets of the pure undecorated 14-PF GMPCPP-MT (red) and 14-PF GDP-MT (orange) are also shown for comparison (same for *C*). (*B*) Plot of layer line profiles for the reconstructions of the two classes observed in the dataset shown in *A*. The layer line profiles of undecorated GMPCPP- and GDP-MT reconstructions are also shown for comparison (same for *D*). (*C*) Histogram of layer line positions for each MT segment in the dataset of EB3 washed GMPCPP-MTs (only 14-PF MTs are plotted in blue). (*D*) Plot of layer line profiles for the reconstructions of two classes present in the dataset of EB3 washed GMPCPP-MTs (14-PF). (*E* and *F*) Top view of the 3D reconstructions of class 1 and class 2, respectively. α-Tubulin, β-tubulin, and EB3 densities are shown in green, blue, and orange, respectively.

in the case of the 13-PF GDP-MT (Fig. 3 *A*–*C*). The difference in lateral interactions at the seam may therefore relate to the stability of MTs bound to these nonhydrolyzable GTP analogs (*Discussion*).

EB3 Induces Lattice Compaction of Preformed 14-PF GMPCPP-MTs. Previously, we have shown that when copolymerizing EB3 with GMPCPP-tubulin, EB3 strongly promotes 13-PF MTs (*SI Appendix*, Fig. S1), induces lattice compaction (Fig. 2*C*), and stimulates the hydrolysis of the usually slowly hydrolyzable GMPCPP (31). To further understand the effects of EB3 on the MT lattice, we challenged EB3 with a MT type that is distinct from its favored MT substrate (31). We first applied undecorated GMPCPP-MTs (predominantly 14-PF MTs and with an extended lattice) to the EM grid, and then washed the grid twice with highly concentrated EB3 before blotting and freezing. Under these experimental conditions, while EB3 did not change the PF number distribution of the premade 14-PF GMPCPP-MTs, it was able to bind and induce measurable changes in the lattice in terms of both lattice compaction and lattice twist. Although the plot of lattice spacing for all of the MT segments does not show a bimodal distribution for the EB3-MT coassembly (Fig. 4*C*), using two distinct 3D references (corresponding to an extended GMPCPP-MT and a compacted GDP-MT), we separated the MT segments into two main classes (class 1 and class 2, which contain 30% and 70% of the total number of particles, respectively). Class 1 had an extended MT lattice that is very similar to the undecorated GMPCPP-MT (Figs. 2*D* and 4*D*), and had weak density corresponding to EB3 (Fig. 4*E*). In contrast, class 2 had a partially compacted lattice (Figs. 2*D* and 4*D*), as well as stronger EB density (Fig. 4*F*). Interestingly, both classes had a significantly more left-handed MT-lattice than the undecorated GMPCPP-MT (Fig. 2*D*). Unfortunately, the limited resolution due to sample heterogeneity did not allow us to visualize whether the GMPCPP at the E-site of the partially compacted class 2 had been hydrolyzed.

These results indicate that a few EB3 molecules can affect MT lattice twist, but only a larger number of bound EB proteins can cause compaction and likely hydrolysis. The fact that particles from the same MT typically go to the same class after sorting suggests a cooperative effect once a certain number of EB proteins bind, likely mediated by a lattice switch into a conformation (the compacted state) that further facilitates EB binding. This model is consistent with the observation that higher concentration of EBs reduced the maturation time of MTs before a catastrophe (34).

Discussion

GTP Analogs and What They Represent for MT Structure and Dynamics. As in the biochemical study of any GTPase, the study of tubulin has involved the use of nonhydrolyzable GTP analogs to dissect its function. GTPγS proved to have strange properties on tubulin assembly, somehow behaving more like GDP than GTP concerning its incapacity to nucleate MT formation (35, 39, 40). The synthesis and use of GMPCPP, a slowly hydrolyzable analog with reasonable affinity for the tubulin E-site that can promote MT assembly, showed it to be a much better mimic of GTP in its effect on tubulin self-assembly (41). The near-atomic resolution structures of undecorated MTs discussed herein provide insights into how the two GTP analogs, GMPCPP and GTPγS, can have dramatically different effects on MT structure. The GMPCPP-bound MT has an extended lattice, while GTPγS-bound MT has a compacted lattice, even in the absence of EB protein. Thus, the GTPγS state of MTs appears more similar to the GDP than the GTP state, a structural result that parallels what is seen in some functional studies with this analog. Because GDP and GTPγS are, nevertheless, not identical in their effect on the MT as observed functionally and structurally (see below), we have proposed that GTPγS mimics a transition state in the nucleotide hydrolysis cycle, probably a GDP-P_i state (31). Consistent with this proposal, high-resolution fluorescence microscopy has recently shown that EB1, which favors GTPγS-MTs as its substrate, binds to a region at the MT growing end that lags several tens of nanometers behind XMAP215 (34), which binds to the extreme end of MT, where the tubulin is presumably in the GTP state.

With regards to the state of GMPCPP-MTs, we have at least three major reasons that lead us to believe that the GMPCPP-MT is a good mimic of a true GTP state, as originally proposed (41). First, both GTP-tubulin and GMPCPP-tubulin are relatively good nucleators, while tubulin in other nucleotide states (GDP and GTPγS) is not. Second, the GMPCPP-MT has a longitudinal interdimer distance, which depends on the nucleotide state at the E-site, that is closer to the mostly invariable intradimer distance (reflecting the constant GTP at the N-site), than that of the GDP- or GTPγS-MTs (Fig. 2*B* and *SI Appendix*, Table S2). Finally, TPX2, a spindle assembly factor that is known to strongly promote MT nucleation (42, 43), probably by stabilizing early nucleation intermediates, shows strong binding specificity for both GMPCPP-MT seeds and the growing ends of MTs in vitro (43). These observations suggest that there are common structural features among GMPCPP-MTs, the MT growing ends, and early nucleation intermediates, with the latter two presumably existing in a GTP state.

Effect of GTP Hydrolysis on MT Structure: Strain and the Seam. Our structural studies comparing MTs in the GMPCPP and GDP states have shown an ∼2-Å lattice compaction upon GTP hydrolysis, which occurs at the polymerization interface between two tubulin dimers (30, 31). This apparent lattice compaction is due to an internal domain rearrangement of every α-tubulin, consisting of a relative rotation of the intermediate domain and the C-terminal helices of α-tubulin with respect to its N-terminal domain. Interestingly, this rotation from the GMPCPP to the GDP state is in the opposite direction from that observed in the proposed "ground state" represented by the crystal structures of unpolymerized tubulin (38, 44), suggesting that GTP hydrolysis generates mechanical strain that is stored in the MT lattice.

In addition to its effect on the lattice compaction (as measured by dimer rise) just described, GTP hydrolysis has other structural consequences that are likely to be relevant for our understanding of MT dynamic instability. These include changes in lattice twist (as measured by dimer twist) and in the lateral contacts at the seam.

When comparing MTs in the same nucleotide state but with different PF numbers (e.g., 13-PF vs. 14-PF), the structures are very similar at the PF level, although the PFs run with a different skew angle with respect to the MT axis (also referred to as "supertwist," and mathematically related to the dimer twist). This skew angle generates the classic moiré pattern observed over long distances (45, 46) that is predicted by the "MT lattice accommodation model" proposed more than 25 y ago by Chrétien and Wade (14). On the other hand, comparison of MTs with the same PF number but in different nucleotide states (e.g., GTPγS vs. GDP) shows that dimer twist changes slightly (31) (Fig. 5*A*). This small shift between two longitudinally interacting tubulin dimers within the PF is likely due to the subtle rearrangement of hydrogen bonds at the E-site. Such a small shift accumulates over long distances, causing the PF to run at a slightly different skew angle (Fig. 5*A*). Thus, both nucleotide state and PF number can alter the skew angle of PFs, which will inevitably change the structural details of the lateral contacts that hold the lattice together against strain, and therefore may affect the overall stability of the MT lattice.

The lateral interactions at the seam may be a direct readout of the overall stability of the MT. We have observed that GDP-MTs are less "cylindrically" symmetric than the GMPCPP and GTPγS MTs (both of which are stable states). In GDP-MTs, the positions of the two PFs across the seam are further apart from each other than those observed for other PF pairs (Fig. 3). It is likely that the α–β interaction at the seam is always intrinsically weaker than the homotypic (α–α or β–β) interactions at nonseam locations, regardless of the nucleotide state. Our studies indicate that when the MT lattice is placed under stress following GTP hydrolysis, this strain is first manifested in the "stretching" of the seam. Based on this observation, we propose that the seam would likely be the first place to crack open in a MT catastrophe event. Losing 1 of the ∼13 lateral interactions that act as a whole to counteract the intrinsic curling tendency of individual PFs would then trigger the outward pealing of other PFs, as is often observed at the ends of depolymerizing MTs (47). Consistent with this idea, we have previously described how the MT-stabilizing agent peloruside, which binds across both homotypic β–β interfaces and heterotypic α–β interfaces, also brings the two PFs across the seam closer to each other (48).

Effect of EB Binding on MT Structure and Stability. In living cells, EBs track with growing MT ends, recognizing a structural state of the MT lattice that is dependent on its nucleotide content. Biophysical and structural studies indicate that EBs preferentially bind a state that is best mimicked in vitro by GTPγS-MT. Despite the fact that both are compacted states, the GDP and GTPγS MT states are not identical. The 13-PF GTPγS-MT has a dimer twist (−0.1°) that is different from both the 13-PF GMPCPP-MT (0.2°) or the GDP-MT (0.1°) (Figs. 2*C* and 5*B* and *SI Appendix*, Table S2). The unique dimer twist observed for GTPγS is likely to be recognized by EB proteins, which bind four tubulin dimers across two PFs and thus are particularly sensitive to PF skew.

By comparing the three nucleotide states (GMPCPP, GDP, and GTPγS) of MTs with and without bound EB3, there is a clear trend that, at least at the high concentrations used in the cryo-EM studies, EB3 introduces an additional left-handed lattice twist to whatever MT lattice it binds (even for 14-PF MTs). EB3 also induces lattice compaction, except when added to a lattice that is already fully compacted (Figs. 2 *C* and *D* and 5*B*). Very similar effects on MT lattice twist by the yeast homologs, Bim1 and Mal3,

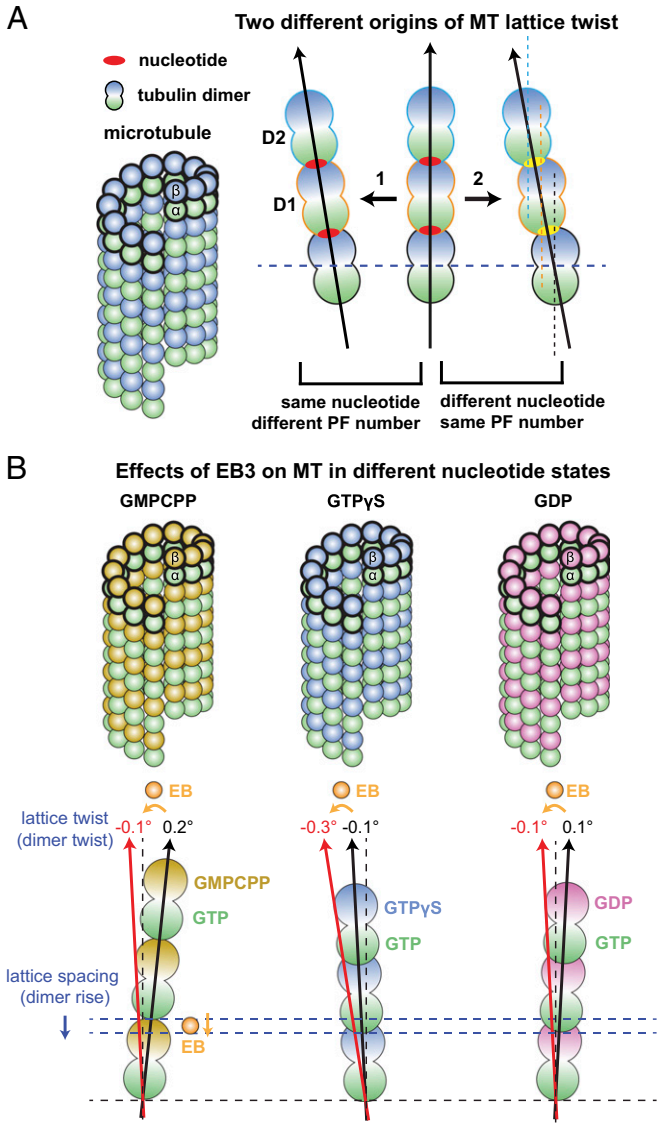

Fig. 5. Cartoon diagram of the different origins of lattice twist and the effect of EB3 on MTs in different nucleotide states. (*A*) Relationships between nucleotide state, PF number, and lattice twist (or PF skewing). (1) MTs with the same nucleotide but different PF numbers will naturally run at a different skew angle with respect to the MT vertical axis, but the tubulin structures are very similar at the PF level. (2) MTs with the same PF number but different nucleotides have a small amount of shift between two longitudinally interacting tubulin dimers along the PF. Such a small shift also accumulates over a long distance, causing the PF to run at a slightly different skew angle. (*B*) In each MT nucleotide state (GMPCPP, GTPγS, and GDP), EB3 generates a left-handed lattice twist (measured as dimer twist). EB3 also induces lattice compaction of GMPCPP-MT.

have also been reported recently (11, 12, 49). In the case of EB3, it appears that the MT conformation for maximal EB3 binding is a 13-PF MT with a compacted lattice (dimer rise of around 81.5 Å) as well as a relatively large left-handed lattice twist (dimer twist of around −0.3°) (Figs. 2*C* and 5*B* and *SI Appendix*, Table S2). Our structural comparisons (Fig. 5*B*) indicate that 13-PF GTPγS-MTs have the intrinsic capacity to fully accommodate this optimal EB binding site, and consequently have the highest affinity for EB3 (10, 35). However, 13-PF GMPCPP-MTs and GDP-MTs can only be partially modulated by EB3 toward its preferred lattice conformation (31), even when EB3 is in excess, likely due to the suboptimal binding pocket for EB3, which spans four tubulin dimers across both longitudinal and lateral interfaces, in these alternative MT lattices.

Thus, the complex effect of EB proteins on MT dynamics is likely to be rooted in the duality of EB recognition of, and effect on, the MT lattice. As just mentioned, our structures show that EB binding leads to lattice compaction of the extended GTP state that is linked to GTP hydrolysis. So far, it is not possible for us to determine, from our structures alone, the causality of the process: Does EB promote compaction that sterically facilitates hydrolysis, or is compaction a result of hydrolysis? Nevertheless, it is apparent that GTP hydrolysis ultimately results in a GDP state with a different lattice twist than that preferred by EB (i.e., that mimicked by GTPγS). Because each EB molecule binds across four tubulin dimers, EB is particularly sensitive to changes in lattice twist. We propose that the lattice twist in the GDP-MT correspond to a low-affinity state for EB that causes it to come off the MT lattice, likely upon P_i release. The combination of effects on MT lattice that we see due to EB binding and nucleotide state provides a structural framework for a mechanistic understanding of the end-tracking behavior of EB proteins.

A Lattice-Centric Model of MT Dynamic Instability and Its Regulation. A number of studies have shown that the structural state of the MT lattice can be modulated by different binding partners, especially when they are present in the high concentrations typically used for cryo-EM studies. The effects seen for these proteins further support a previously proposed model of structural plasticity for tubulin and MTs (50). It appears that proteins that bind across the interdimer interface, such as EB proteins (10, 31), doublecortin (7, 51), or TPX2 (37), have stronger influence on MT lattice and MT dynamics than MT-binding proteins that bind within the tubulin dimer, such as dynein (52, 53), kinesin (15, 16), TTLL7 (54), PRC1 (55, 56), or WHAMM (57).

In addition to sensing the subtle lattice differences in straight MTs, it has been observed that several MAPs, such as TPX2 (43) or doublecortin (58, 59), can preferentially accumulate at curved regions of MTs, which can arise from deformations due to mechanical forces. Such curved MT regions may provide unique lattice configurations that are different from those in straight regions. For example, as recently proposed by Wittmann and coworkers (59), the convex or the concave side of the curvature may provide slightly larger or smaller dimer spacing, respectively, that can be preferentially recognized by MT binding partners.

It is believed that growing MT ends and early nucleation intermediates may share similar structural features, probably the open sheet structure (60–63). Such lattice conformation, which will be absent in the MT shaft, can be recognized by certain MT binding proteins. In fact, consistent models have been proposed recently to explain the plus-end recognition by EB proteins (64–66), the early nucleation intermediates recognition by TPX2 (37, 43) and doublecortin (58, 67), and also the minus-end accumulation by CAMSAP (66).

We propose a MT lattice-centric model in which the MT lattice, either in straight or curved regions, serves as a platform in the cell to integrate multiple internal tubulin signals (i.e., nucleotide state, chemical modifications, and others) and outside signals (i.e., binding of MAPs, binding of stabilizing/destabilizing drugs or mechanical forces), and the resulting global lattice rearrangement in turn affects the affinity of its binding partners. In this way, the dynamics properties of MTs can be exquisitely regulated by the combinatorial and sometimes sequential binding of associated factors.

Experimental Procedures

Protein Purification. The human EB3 monomeric construct (residues 1–200) was expressed in BL21-CodonPlus-(DE3)-RIL cells and purified using His-tag affinity purification and size-exclusion, following a previously published protocol (31). Porcine brain tubulin was purchased from Cytoskeleton.

Cryo-EM Sample Preparation. The kinesin-decorated and undecorated GMPCPP-MT samples were prepared as previously described (30, 31). We typically snap-freeze 5-μL aliquots of GMPCPP-loaded tubulin (that has been through one polymerization–depolymerization cycle) at 3 mg/mL for future use (e.g., to make GMPCPP-MT seeds). The undecorated GDP-MTs were made by polymerizing a 5-μL aliquot of 10-mg/mL dynamic porcine MTs in CB1 buffer (80 mM Pipes pH 6.8, 1 mM EGTA, 1 mM $MgCl_2$, 1 mM GTP, 10% glycerol) for 45 min at 37 °C. This was followed by a 20 min 16,000 × *g* centrifugation step at 37 °C to pellet the "assembly competent" MTs. The supernatant was discarded and the GDP-MT pellet was resuspended in 5 μL of warm CB1 buffer supplemented with 0.05% Nonident P-40, and repolymerized for 15–20 min before plunge-freezing in liquid ethane.

GTPγS-MTs were obtained using the following procedure, which is adapted from a previously published protocol (35, 68). First, we prepared GMPCPP-MT seeds from a frozen aliquot of GMPCPP-tubulin by incubation at 37 °C, stopping the polymerization by 10-fold dilution after just 2 min to obtain relatively short MT seeds. The GMPCPP-MT seeds were pelleted and resuspended in an equal volume of warm BRB80 buffer without GMPCPP. Next, Porcine tubulin powder (Cytoskeleton) was reconstituted to 10 mg/mL in CB1 buffer. After polymerizing MTs at 37 °C for 45 min followed by centrifugation at 17,000 × *g* for 15 min, MT pellets was resuspended in cold EM buffer with a lower Mg^{2+} concentration (80 mM Pipes, pH 6.8, 1 mM EGTA, 0.2 mM $MgCl_2$, 1 mM DTT, 0.05% Nonidet P-40) supplemented with 1 mM GTPγS (Roche), which causes MT depolymerization and tubulin E-site nucleotide exchange. After 20 min, the GTPγS-loaded tubulin was diluted to 5-mg/mL concentration, and 15 μL of GTPγS-tubulin was warmed up to room temperature and mixed with 1 μL of preformed GMPCPP-MT seeds (~0.3 mg/mL). The sample was allowed to polymerize at 37 °C in EM buffer for about 45 min before EM grid preparation.

To freeze the undecorated MTs, 3 μL of MT sample (diluted to ~0.2 mg/mL) was applied to a glow-discharged C-flat 1.2/1.3–4C holey carbon EM grid (Protochips). After 30-s incubation time inside a Vitrobot (FEI) set at 25 °C for GMPCPP-MTs or 37 °C for GTPγS-MTs and dynamic MTs, the grid was blotted for 4 s and plunged in liquid ethane.

For the experiment using preformed GMPCPP-MTs that were washed with EB3, we desalted EB3 into cold EM buffer using a Zeba Micro Spin desalting column (Thermo Scientific) and the sample was clarified by ultracentrifugation. Next, 3 μL of the GMPCPP-MT sample was first absorbed to a glow-discharged EM grid. After 30-s incubation inside a Vitrobot set at 25 °C, the grid was washed twice with 3 μL of EB3 at 30-μM concentration (30-s incubation each time), before blotting and vitrification in liquid ethane.

Cryo-EM Data Collection. Three datasets (undecorated GMPCPP-MT, undecorated GDP-MT, and kinesin decorated GMPCPP-MT) were collected using a 300-keV Titan Krios at the University of California, San Francisco cryo-EM facility. A bigger dataset of undecorated GMPCPP-MT was collected using a 300-keV Titan Krios equipped with a Cs-corrector and a Gatan Image Filter (GIF) at the Center for Cellular Imaging in Washington University in St. Louis. All other datasets were collected using a 300-keV low-base Titan microscope (FEI) located at University of California, Berkeley. All of the data were collected using a K2 Summit direct electron detector (Gatan), in counting or superresolution mode, with a dose rate of eight to nine electrons per pixel per second. All of the samples were imaged under parallel illumination conditions, with a beam diameter of ~2 μm on the specimen. A defocus range from −0.5 to −2.5 μm was used. The data were collected using Leginon (69), SerialEM (70), and EPU (FEI) at University of California, Berkeley, University of California, San Francisco, and Washington University in St. Louis, respectively. The data-collection statistics are listed in *SI Appendix*, Table S1.

Image Processing. Drift correction for each movie stack was performed using the MotionCor2 program (71). Then the contrast transfer function parameters were estimated from the motion-corrected micrographs using Gctf (72). In the next step, we manually selected MTs from the motion-corrected micrographs using the APPION image-processing suite (73). Then the selected MT images were computationally cut into overlapping boxes, with an ~80-Å nonoverlapping region (along the MT axis) between adjacent boxes. The initial alignment parameters and PF number for each boxed MT segment were determined using multireference alignment in EMAN1 (74). MT segments with the same PF number were grouped and subjected to further structural refinement in FREALIGN v9 (75). After that, we used a recently established data-processing protocol to determine the αβ-tubulin register and seam location for each boxed MT segment (36). The kinesin/EB3 decorated MTs and undecorated MTs were processed using exactly the same set of scripts, although in the case of undecorated MTs, a good reference model (resolution better than 6 Å) with clear distinction of α-, β-tubulin density was needed. Finally, 3D reconstructions (assuming either MT pseudohelical symmetry or no symmetry) were performed using FREALIGN (sym = HP or sym = 0). During the reconstruction process, particles are weighted based on their similarity scores with respect to the reference model, and 20% "bad" particles with the lowest scores were discarded. Typically, a few (fewer than 5) rounds of refinement were needed to reach a stable reconstruction. For each MT state, the helical symmetry parameters (axial rise and azimuthal twist) corresponding to the 3-start helix or 13-start helix (i.e., dimer rise and dimer twist) of the MT were measured from the C1 reconstruction using the *relion_helix_toolbox* program in RELION v2.1 (76), which gave results consistent with those we previously obtained (31) using the hsearch_lorentz program in the IHRSR package (77). The final resolution for each reconstruction (*SI Appendix*, Table S1) was estimated by calculating the Fourier shell correlation (FSC) of the "good" protofilament (36) segment containing three adjacent tubulin dimers from the odd and even maps, using a FSC 0.143 criterion (FSC calculations based on whole microtubule reconstructions tend to give underestimated resolution).

To separate the MTs based on their lattice spacing, we compute the MT "superparticles" by averaging every seven neighboring MT raw particles together using their alignment parameters obtained from FREALIGN (36). This is based on the idea that due to the slow supertwist of MT, neighboring MT particles represent very similar views of the MT, even for the 14-PF MTs. In the superparticles, the signal-to-noise ratio is greatly improved, therefore allowing us to precisely measure the spacing of layer lines in the 2D Fourier Transform of the image, which corresponds to the lattice spacing in real space. Considering the fact that MTs may lie slightly tilted with respect to the grid plane, the measured layer line spacing is corrected by multiplying the cosine of this tilt angle (θ angle in FREALIGN convention). In the case of GTPγS MTs extended from GMPCPP-MT seeds, based on the shape of the histogram of the layer line spacing for all of the superparticles, which displays a bimodal distribution, a cut-off value of 99 was determined to split the MT dataset into two homogenous subgroups (Fig. 4*A*). In the case of preformed GMPCPP-MTs washed with EB3, it's hard to determine a cut-off value based on the histogram (Fig. 4*C*); therefore, only multireference sorting was performed for this dataset.

Atomic Model Building and Refinement. The atomic models of undecorated GMPCPP, GDP, and GTPγS-MT were built in COOT (78), based on the high-resolution cryo-EM density maps and our previously deposited atomic models (PDB ID codes 3JAT, 3JAS, and 3JAK for GMPCPP, GDP, and GTPγS-MT, respectively) (31). Torsion angle, planar peptide, and Ramachandran restraints were used during the building process in COOT.

For each MT reconstruction, the model of one αβ-tubulin dimer built in COOT was fitted as a rigid-body into the MT lattice to generate an initial model containing six tubulin dimers that was subsequently refined with REFMAC v5.8 adapted for cryo-EM (79), following a previously described protocol (31). Secondary structure and reference restraints generated with ProSMART (80) were used throughout the refinement process. During refinement, local symmetry restraints were used to restrain corresponding interatomic distances in symmetry-related molecules. These local symmetry restraints are functionally analogous to noncrystallographic symmetry restraints used during crystallographic refinement (81).

Molecular Graphics. All structural figures were generated using UCSF Chimera software (82, 83).

Data Deposition. The following cryo-EM maps have been deposited in the Electron Microscopy Data Bank (EMDB): undecorated GMPCPP-MT (EMD-7973), undecorated GDP-MT (EMD-7974), undecorated GTPγS-MT (EMD-7975), and EB3-washed GMPCPP-MT, class 1 and 2 (EMD-7976 and EMD-7977). The refined atomic models for the undecorated GMPCPP-, GDP-, and GTPγS-MT have been deposited in the Protein Data Bank (PDB) with ID codes 6DPU, 6DPV, and 6DPW, respectively.

ACKNOWLEDGMENTS. We thank Sebastian Maurer for guidance of the assembly of GTPγS-MT in the absence of end-binding proteins; Patricia Grob for EM support; Tom Houweling and Abhiram Chintangal for computer support; David Bulkley and Alexander Myasnikov for assistance in data collection at the University of California, San Francisco; and James Fitzpatrick and Michael Rau for assistance in data collection at Washington University in St. Louis, Center for Cellular Imaging. This work was funded by National Institute of General Medical Sciences Grant GM051487 (to E.N.). B.L. is supported by National Science Foundation-Graduate Research Fellowships Program 1106400. E.N. is a Howard Hughes Medical Institute investigator.

1. Unger E, Böhm KJ, Vater W (1990) Structural diversity and dynamics of microtubules and polymorphic tubulin assemblies. *Electron Microsc Rev* 3:355–395.
2. McIntosh JR, Morphew MK, Grissom PM, Gilbert SP, Hoenger A (2009) Lattice structure of cytoplasmic microtubules in a cultured mammalian cell. *J Mol Biol* 394: 177–182.
3. Chaaban S, Brouhard GJ (2017) A microtubule bestiary: Structural diversity in tubulin polymers. *Mol Biol Cell* 28:2924–2931.
4. Zheng Y, Wong ML, Alberts B, Mitchison T (1995) Nucleation of microtubule assembly by a gamma-tubulin-containing ring complex. *Nature* 378:578–583.
5. Moritz M, Braunfeld MB, Sedat JW, Alberts B, Agard DA (1995) Microtubule nucleation by gamma-tubulin-containing rings in the centrosome. *Nature* 378: 638–640.
6. Kollman JM, Merdes A, Mourey L, Agard DA (2011) Microtubule nucleation by γ-tubulin complexes. *Nat Rev Mol Cell Biol* 12:709–721.
7. Moores CA, et al. (2004) Mechanism of microtubule stabilization by doublecortin. *Mol Cell* 14:833–839.
8. des Georges A, et al. (2008) Mal3, the *Schizosaccharomyces pombe* homolog of EB1, changes the microtubule lattice. *Nat Struct Mol Biol* 15:1102–1108.
9. Vitre B, et al. (2008) EB1 regulates microtubule dynamics and tubulin sheet closure in vitro. *Nat Cell Biol* 10:415–421.
10. Maurer SP, Fourniol FJ, Bohner G, Moores CA, Surrey T (2012) EBs recognize a nucleotide-dependent structural cap at growing microtubule ends. *Cell* 149: 371–382.
11. Howes SC, et al. (2017) Structural differences between yeast and mammalian microtubules revealed by cryo-EM. *J Cell Biol* 216:2669–2677.
12. Howes SC, et al. (2017) Structural and functional differences between porcine brain and budding yeast microtubules. *Cell Cycle* 17:278–287.
13. Mandelkow EM, Schultheiss R, Rapp R, Müller M, Mandelkow E (1986) On the surface lattice of microtubules: Helix starts, protofilament number, seam, and handedness. *J Cell Biol* 102:1067–1073.
14. Chrétien D, Wade RH (1991) New data on the microtubule surface lattice. *Biol Cell* 71: 161–174.
15. Kikkawa M, Ishikawa T, Nakata T, Wakabayashi T, Hirokawa N (1994) Direct visualization of the microtubule lattice seam both in vitro and in vivo. *J Cell Biol* 127: 1965–1971.
16. Sosa H, Milligan RA (1996) Three-dimensional structure of ncd-decorated microtubules obtained by a back-projection method. *J Mol Biol* 260:743–755.
17. Sandblad L, et al. (2006) The *Schizosaccharomyces pombe* EB1 homolog Mal3p binds and stabilizes the microtubule lattice seam. *Cell* 127:1415–1424.
18. Deng X, et al. (2017) Four-stranded mini microtubules formed by *Prosthecobacter* BtubAB show dynamic instability. *Proc Natl Acad Sci USA* 114:E5950–E5958.
19. Wang F, et al. (2017) A structural model of flagellar filament switching across multiple bacterial species. *Nat Commun* 8:960.
20. Nogales E, Wolf SG, Downing KH (1998) Structure of the alpha beta tubulin dimer by electron crystallography. *Nature* 391:199–203.
21. Löwe J, Li H, Downing KH, Nogales E (2001) Refined structure of alpha beta-tubulin at 3.5 A resolution. *J Mol Biol* 313:1045–1057.
22. Menéndez M, Rivas G, Díaz JF, Andreu JM (1998) Control of the structural stability of the tubulin dimer by one high affinity bound magnesium ion at nucleotide N-site. *J Biol Chem* 273:167–176.
23. Nogales E, Whittaker M, Milligan RA, Downing KH (1999) High-resolution model of the microtubule. *Cell* 96:79–88.
24. Mitchison T, Kirschner M (1984) Dynamic instability of microtubule growth. *Nature* 312:237–242.
25. Drechsel DN, Kirschner MW (1994) The minimum GTP cap required to stabilize microtubules. *Curr Biol* 4:1053–1061.
26. Caplow M, Shanks J (1996) Evidence that a single monolayer tubulin-GTP cap is both necessary and sufficient to stabilize microtubules. *Mol Biol Cell* 7:663–675.
27. Schiff PB, Fant J, Horwitz SB (1979) Promotion of microtubule assembly in vitro by taxol. *Nature* 277:665–667.
28. Dumontet C, Jordan MA (2010) Microtubule-binding agents: A dynamic field of cancer therapeutics. *Nat Rev Drug Discov* 9:790–803.
29. Ojima I, Kumar K, Awasthi D, Vineberg JG (2014) Drug discovery targeting cell division proteins, microtubules and FtsZ. *Bioorg Med Chem* 22:5060–5077.
30. Alushin GM, et al. (2014) High-resolution microtubule structures reveal the structural transitions in αβ-tubulin upon GTP hydrolysis. *Cell* 157:1117–1129.
31. Zhang R, Alushin GM, Brown A, Nogales E (2015) Mechanistic origin of microtubule dynamic instability and its modulation by EB proteins. *Cell* 162:849–859.
32. Akhmanova A, Steinmetz MO (2008) Tracking the ends: A dynamic protein network controls the fate of microtubule tips. *Nat Rev Mol Cell Biol* 9:309–322.
33. Honnappa S, et al. (2009) An EB1-binding motif acts as a microtubule tip localization signal. *Cell* 138:366–376.
34. Maurer SP, et al. (2014) EB1 accelerates two conformational transitions important for microtubule maturation and dynamics. *Curr Biol* 24:372–384.
35. Maurer SP, Bieling P, Cope J, Hoenger A, Surrey T (2011) GTPgammaS microtubules mimic the growing microtubule end structure recognized by end-binding proteins (EBs). *Proc Natl Acad Sci USA* 108:3988–3993.
36. Zhang R, Nogales E (2015) A new protocol to accurately determine microtubule lattice seam location. *J Struct Biol* 192:245–254.
37. Zhang R, Roostalu J, Surrey T, Nogales E (2017) Structural insight into TPX2-stimulated microtubule assembly. *eLife* 6:e30959.
38. Brouhard GJ, Rice LM (2014) The contribution of αβ-tubulin curvature to microtubule dynamics. *J Cell Biol* 207:323–334.
39. Hamel E, Lin CM (1984) Guanosine 5′-O-(3-thiotriphosphate), a potent nucleotide inhibitor of microtubule assembly. *J Biol Chem* 259:11060–11069.
40. Roychowdhury S, Gaskin F (1986) Magnesium requirements for guanosine 5′-O-(3-thiotriphosphate) induced assembly of microtubule protein and tubulin. *Biochemistry* 25:7847–7853.
41. Hyman AA, Salser S, Drechsel DN, Unwin N, Mitchison TJ (1992) Role of GTP hydrolysis in microtubule dynamics: Information from a slowly hydrolyzable analogue, GMPCPP. *Mol Biol Cell* 3:1155–1167.
42. Wieczorek M, Bechstedt S, Chaaban S, Brouhard GJ (2015) Microtubule-associated proteins control the kinetics of microtubule nucleation. *Nat Cell Biol* 17:907–916.
43. Roostalu J, Cade NI, Surrey T (2015) Complementary activities of TPX2 and chTOG constitute an efficient importin-regulated microtubule nucleation module. *Nat Cell Biol* 17:1422–1434.
44. Rice LM, Montabana EA, Agard DA (2008) The lattice as allosteric effector: Structural studies of alphabeta- and gamma-tubulin clarify the role of GTP in microtubule assembly. *Proc Natl Acad Sci USA* 105:5378–5383.
45. Mandelkow EM, Mandelkow E (1985) Unstained microtubules studied by cryo-electron microscopy. Substructure, supertwist and disassembly. *J Mol Biol* 181: 123–135.
46. Chrétien D, Kenney JM, Fuller SD, Wade RH (1996) Determination of microtubule polarity by cryo-electron microscopy. *Structure* 4:1031–1040.
47. Mandelkow EM, Mandelkow E, Milligan RA (1991) Microtubule dynamics and microtubule caps: A time-resolved cryo-electron microscopy study. *J Cell Biol* 114: 977–991.
48. Kellogg EH, et al. (2017) Insights into the distinct mechanisms of action of taxane and non-taxane microtubule stabilizers from cryo-EM structures. *J Mol Biol* 429: 633–646.
49. von Loeffelholz O, et al. (2017) Nucleotide- and Mal3-dependent changes in fission yeast microtubules suggest a structural plasticity view of dynamics. *Nat Commun* 8: 2110.
50. Kueh HY, Mitchison TJ (2009) Structural plasticity in actin and tubulin polymer dynamics. *Science* 325:960–963.
51. Fourniol FJ, et al. (2010) Template-free 13-protofilament microtubule-MAP assembly visualized at 8 A resolution. *J Cell Biol* 191:463–470.
52. Mizuno N, et al. (2004) Dynein and kinesin share an overlapping microtubule-binding site. *EMBO J* 23:2459–2467.
53. Redwine WB, et al. (2012) Structural basis for microtubule binding and release by dynein. *Science* 337:1532–1536.
54. Garnham CP, et al. (2015) Multivalent microtubule recognition by tubulin tyrosine ligase-like family glutamylases. *Cell* 161:1112–1123.
55. Subramanian R, et al. (2010) Insights into antiparallel microtubule crosslinking by PRC1, a conserved nonmotor microtubule binding protein. *Cell* 142:433–443.
56. Kellogg EH, et al. (2016) Near-atomic cryo-EM structure of PRC1 bound to the microtubule. *Proc Natl Acad Sci USA* 113:9430–9439.
57. Liu T, et al. (2017) Structural insights of WHAMM's interaction with microtubules by cryo-EM. *J Mol Biol* 429:1352–1363.
58. Bechstedt S, Lu K, Brouhard GJ (2014) Doublecortin recognizes the longitudinal curvature of the microtubule end and lattice. *Curr Biol* 24:2366–2375.
59. Ettinger A, van Haren J, Ribeiro SA, Wittmann T (2016) Doublecortin is excluded from growing microtubule ends and recognizes the GDP-microtubule lattice. *Curr Biol* 26: 1549–1555.
60. Kirschner MW, Honig LS, Williams RC (1975) Quantitative electron microscopy of microtubule assembly in vitro. *J Mol Biol* 99:263–276.
61. Chrétien D, Fuller SD, Karsenti E (1995) Structure of growing microtubule ends: Two-dimensional sheets close into tubes at variable rates. *J Cell Biol* 129:1311–1328.
62. Wang HW, Long S, Finley KR, Nogales E (2005) Assembly of GMPCPP-bound tubulin into helical ribbons and tubes and effect of colchicine. *Cell Cycle* 4: 1157–1160.
63. Mozziconacci J, Sandblad L, Wachsmuth M, Brunner D, Karsenti E (2008) Tubulin dimers oligomerize before their incorporation into microtubules. *PLoS One* 3: e3821.
64. Wang HW, Nogales E (2005) Nucleotide-dependent bending flexibility of tubulin regulates microtubule assembly. *Nature* 435:911–915.
65. Guesdon A, et al. (2016) EB1 interacts with outwardly curved and straight regions of the microtubule lattice. *Nat Cell Biol* 18:1102–1108.
66. Atherton J, et al. (2017) A structural model for microtubule minus-end recognition and protection by CAMSAP proteins. *Nat Struct Mol Biol* 24:931–943.
67. Bechstedt S, Brouhard GJ (2012) Doublecortin recognizes the 13-protofilament microtubule cooperatively and tracks microtubule ends. *Dev Cell* 23:181–192.
68. Maurer SP, Fourniol FJ, Hoenger A, Surrey T (2014) Seeded microtubule growth for cryoelectron microscopy of end-binding proteins. *Methods Mol Biol* 1136: 247–260.
69. Suloway C, et al. (2005) Automated molecular microscopy: The new Leginon system. *J Struct Biol* 151:41–60.
70. Mastronarde DN (2005) Automated electron microscope tomography using robust prediction of specimen movements. *J Struct Biol* 152:36–51.
71. Zheng SQ, et al. (2017) MotionCor2: Anisotropic correction of beam-induced motion for improved cryo-electron microscopy. *Nat Methods* 14:331–332.
72. Zhang K (2016) Gctf: Real-time CTF determination and correction. *J Struct Biol* 193: 1–12.
73. Lander GC, et al. (2009) Appion: An integrated, database-driven pipeline to facilitate EM image processing. *J Struct Biol* 166:95–102.
74. Ludtke SJ, Baldwin PR, Chiu W (1999) EMAN: Semiautomated software for high-resolution single-particle reconstructions. *J Struct Biol* 128:82–97.
75. Grigorieff N (2007) FREALIGN: High-resolution refinement of single particle structures. *J Struct Biol* 157:117–125.

76. Kimanius D, Forsberg BO, Scheres SH, Lindahl E (2016) Accelerated cryo-EM structure determination with parallelisation using GPUs in RELION-2. *eLife* 5:e18722.
77. Egelman EH (2000) A robust algorithm for the reconstruction of helical filaments using single-particle methods. *Ultramicroscopy* 85:225–234.
78. Emsley P, Lohkamp B, Scott WG, Cowtan K (2010) Features and development of Coot. *Acta Crystallogr D Biol Crystallogr* 66:486–501.
79. Brown A, et al. (2015) Tools for macromolecular model building and refinement into electron cryo-microscopy reconstructions. *Acta Crystallogr D Biol Crystallogr* 71:136–153.
80. Nicholls RA, Long F, Murshudov GN (2012) Low-resolution refinement tools in REFMAC5. *Acta Crystallogr D Biol Crystallogr* 68:404–417.
81. Murshudov GN, et al. (2011) REFMAC5 for the refinement of macromolecular crystal structures. *Acta Crystallogr D Biol Crystallogr* 67:355–367.
82. Pettersen EF, et al. (2004) UCSF Chimera—A visualization system for exploratory research and analysis. *J Comput Chem* 25:1605–1612.
83. Goddard TD, Huang CC, Ferrin TE (2007) Visualizing density maps with UCSF Chimera. *J Struct Biol* 157:281–287.